ORIGINAL ARTICLE

Bingquan Wang · Selda Oterkus · Erkan Oterkus

Derivation of dual-horizon state-based peridynamics formulation based on Euler–Lagrange equation

Abstract The numerical solution of peridynamics equations is usually done by using uniform spatial discretisation. Although implementation of uniform discretisation is straightforward, it can increase computational time significantly for certain problems. Instead, non-uniform discretisation can be utilised and different discretisation sizes can be used at different parts of the solution domain. Moreover, the peridynamic length scale parameter, horizon, can also vary throughout the solution domain. Such a scenario requires extra attention since conservation laws must be satisfied. To deal with these issues, dual-horizon peridynamics was introduced so that both non-uniform discretisation and variable horizon sizes can be utilised. In this study, dual-horizon peridynamics formulation is derived by using Euler–Lagrange equation for state-based peridynamics. Moreover, application of boundary conditions and determination of surface correction factors are also explained. Finally, the current formulation is verified by considering two benchmark problems including plate under tension and vibration of a plate.

1 Introduction

Peridynamics (PD) has been introduced by Silling [1] to overcome the problems and limitations of classical continuum mechanics (CCM). Amongst these problems, the governing equations of CCM are in partial differential equation form which are not valid along crack surfaces since the displacement field is not continuous at those locations. On the other hand, the governing equations of PD are in integro-differential equation form and do not contain any spatial derivatives. Therefore, they are always applicable regardless of discontinuity in the displacement field. Moreover, CCM does not have a length scale parameter. Hence, it cannot represent non-classical material behaviour which usually appears at micro-scale. Instead, peridynamics is a non-local continuum mechanics formulation and it has a length scale parameter called horizon. As mentioned by dell'Isola et. al. [2,3], the origins of peridynamics go back to Piola.

Since its introduction, there has been a rapid progress in peridynamics research. Since it is a general continuum mechanics formulation, any material system can be analysed by using peridynamics including metals [4], composites [5–7], polycrystalline materials [8–10], concrete [11], ceramics [12], ice [13], graphene [14], etc. It is also possible to perform fatigue analysis in PD theory [15]. Moreover, any type of material behaviour can be incorporated, such as plasticity [16], viscoelasticity [17], and viscoplasticity [18]. In addition, PD can be used for multiphysics analysis since peridynamics equations are also available for thermal field [19,20], electrical field [21], diffusion field [22–25], porous flow [26], etc. PD can also be used for fluid

Communicated by Luca Placidi.

B. Wang · S. Oterkus · E. Oterkus (✉)
Peridynamics Research Centre, Department of Naval Architecture, Ocean and Marine Engineering, University of Strathclyde, Glasgow, UK E-mail: erkan.oterkus@strath.ac.uk

flow simulations [27,28]. Peridynamic formulations for simplified structures, including beams [29,30], plates [31] and shells [32], are also available in the literature. With the advancement of additive manufacturing technologies, fabrication of complex materials such as microstructured materials [33–44] is possible. PD theory can be a suitable alternative for the analysis of microstructured materials.

Analytical solutions of PD equations are not usually possible. Therefore, numerical techniques, especially meshless method, are widely utilised. In majority of the publications in the literature, uniform discretisation is used for spatial discretisation. Although uniform discretisation is simple to implement, for certain applications, it unnecessarily increases computational time since only some parts of the solution domain require a finer discretisation and other parts can be discretised by using a coarser grid. Hence, non-uniform discretisation can be very beneficial in terms of computational time. In addition to non-uniform discretisation, horizon size can also be different at different parts of the solution domain either to reduce the computational time or to capture correct physics of the problem. However, this requires extra care especially to satisfy conservation laws. To accomplish these requirements, Ren et. al. [45,46] introduced dual-horizon peridynamics concept. In this study, we present a different way to derive dual-horizon peridynamics formulation for state-based peridynamics by utilising Euler–Lagrange equations. Moreover, application of boundary conditions and determination of surface correction factors are also explained. Finally, the current formulation is verified by considering two benchmark problems including plate under tension and vibration of a plate.

2 Dual-horizon peridynamics formulation based on Euler–Lagrange equation

In this study, dual-horizon peridynamics formulation is derived based on Euler–Lagrange equation. Peridynamics is a non-local continuum mechanics formulation. Therefore, the body is composed of small volumes called "material points" as shown in Fig. 1.

The equation of motion of a particular material point k at location $\mathbf{x}_{(k)}$ in the initial configuration can be obtained by using Euler–Lagrange equation as [4]

$$\frac{d}{dt}\left(\frac{\partial L}{\partial \dot{\mathbf{u}}_{(k)}}\right) - \frac{\partial L}{\partial \mathbf{u}_{(k)}} = 0 \tag{1}$$

where L is the Lagrangian which represents the difference between the total kinetic energy of the body and the total potential energy of the body, t represents time, $\mathbf{u}_{(k)}$ and $\dot{\mathbf{u}}_{(k)}$ are the displacement and velocity of the material point k. The total kinetic energy of the body can be calculated by summing the kinetic energies of all
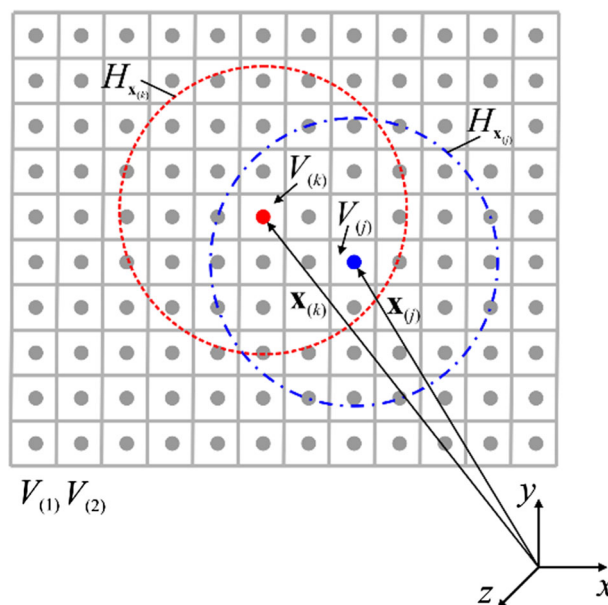

Fig. 1 Material points and the horizon concept [4]

material points in the body as

$$T = \sum_{i=1}^{\frac{1}{2}} \rho_{(i)} \dot{\mathbf{u}}_{(i)} \cdot \dot{\mathbf{u}}_{(i)} V_{(i)} \tag{2}$$

where ρ is the density and $V_{(i)}$ is the volume of the material point i. On the other hand, the total potential energy of the body is the difference between the total strain energy of the body and the energy due to external forces which can be written as

$$U = \sum_{i=1} W_{(i)} V_{(i)} - \sum_{i=1} \left(\mathbf{b}_{(i)} \cdot \mathbf{u}_{(i)} \right) V_{(i)} \tag{3}$$

where W is the strain energy density which can be defined for the material point k as

$$W_{(k)} = \frac{1}{2} \sum_{j=1}^{N_k} \frac{1}{2} \left(\omega_{(k)(j)} \left(\mathbf{y}_{(1^k)} - \mathbf{y}_{(k)}, ..., \mathbf{y}_{(N_k^k)} - \mathbf{y}_{(k)} \right) + \omega_{(j)(k)} \left(\mathbf{y}_{(1^j)} - \mathbf{y}_{(j)}, ..., \mathbf{y}_{(N_j^j)} - \mathbf{y}_{(j)} \right) \right) V_{(j)} \tag{4}$$

with ω being the micropotential arising due to interaction between material points k and j, N_k and N_j represent the number of family members within the horizon of material points k and j, respectively, and $\mathbf{y}$ is the position of the material point in the deformed configuration. Note that micropotentials $\omega_{(k)(j)}$ and $\omega_{(j)(k)}$ do not need to be equal to each other since they have a different domain of influence, horizon (Fig. 1). In Eq. (3), $\mathbf{b}$ is the body load acting on a particular material point. Substituting Eqs. (2) and (3) in Euler–Lagrange equation given in Eq. (1), the equation of motion of the material point k can be obtained as

$$\rho_{(k)} \ddot{\mathbf{u}}_{(k)} = \sum_{j=1}^{N_k} \left(\mathbf{t}_{(k)(j)} - \mathbf{t}_{(j)(k)} \right) V_{(j)} + \mathbf{b}_{(k)} \tag{5}$$

where peridynamic forces given in Eq. (5) can be written in terms of micropotentials between interacting material points, ω, as

$$\mathbf{t}_{kj} = \frac{1}{2} \frac{1}{V_j} \left(\sum_{i=1}^{N_k} \frac{\partial \omega_{ki}}{\partial \left(\mathbf{y}_j - \mathbf{y}_k \right)} V_i \right) \tag{6}$$

$$\mathbf{t}_{jk} = \frac{1}{2} \frac{1}{V_k} \left(\sum_{i=1}^{N_j} \frac{\partial \omega_{ji}}{\partial \left(\mathbf{y}_k - \mathbf{y}_j \right)} V_i \right). \tag{7}$$

For ordinary state-based peridynamics, peridynamic forces can be rewritten for variable size horizon case as

$$\mathbf{t}_{kj} = \alpha_{kj} \left(\frac{2ad\delta_k}{\left| \mathbf{x}_j - \mathbf{x}_k \right|} \theta_k \left(\mathbf{x}_k, t \right) + b \, s_{kj} \right) \frac{\mathbf{y}_j - \mathbf{y}_k}{\left| \mathbf{y}_j - \mathbf{y}_k \right|} \tag{8}$$

$$\mathbf{t}_{jk} = \alpha_{jk} \left(\frac{2ad\delta_j}{\left| \mathbf{x}_j - \mathbf{x}_k \right|} \theta_j \left(\mathbf{x}_j, t \right) + b \, s_{kj} \right) \frac{\mathbf{y}_k - \mathbf{y}_j}{\left| \mathbf{y}_k - \mathbf{y}_j \right|} \tag{9}$$

with

$$\alpha_{kj} = \begin{cases} 1, \omega_{kj} \neq 0 \\ 0, \omega_{kj} = 0 \end{cases} \tag{10}$$

$$\alpha_{jk} = \begin{cases} 1, \omega_{jk} \neq 0 \\ 0, \omega_{jk} = 0 \end{cases} \tag{11}$$
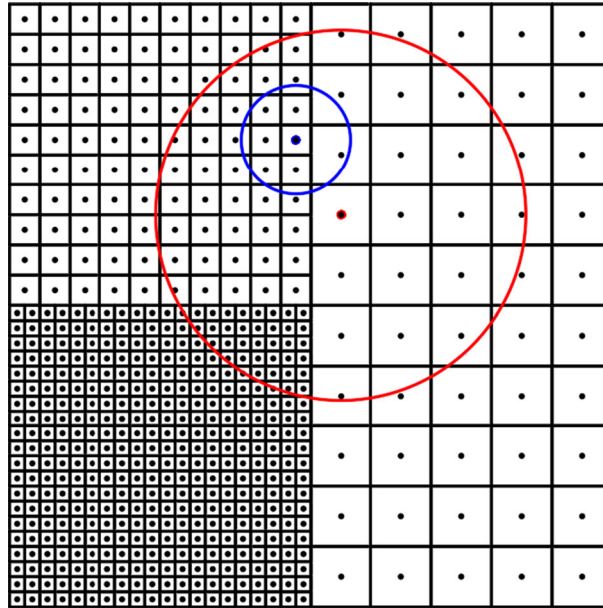
Fig. 2 Non-uniform discretisation with different horizon sizes

and the stretch term can be expressed as

$$s_{kj} = \frac{\left|\mathbf{y}_j - \mathbf{y}_k\right| - \left|\mathbf{x}_j - \mathbf{x}_k\right|}{\left|\mathbf{x}_j - \mathbf{x}_k\right|}. \tag{12}$$

The peridynamic dilatation in Eqs. (8,9) for the material points k and j is defined as

$$\theta_k = \sum_{i=1}^{N_k} d\delta_k s_{ki} V_i \tag{13}$$

$$\theta_j = \sum_{i=1}^{N_j} d\delta_j s_{ji} V_i. \tag{14}$$

The parameters a, b and d are peridynamic parameters which can be expressed in terms of material constants of CCM for an isotropic material as

$$a = \frac{1}{2}(\kappa - 2\mu) \tag{15}$$

$$b = \frac{6\mu}{\pi h \delta^4} \tag{16}$$

$$d = \frac{2}{\pi h \delta^3} \tag{17}$$

with κ and μ being the bulk and shear moduli, respectively, h is the thickness of the two-dimensional domain and δ is the horizon size of a particular material point.

Note that in Eqs. (10) and (11), the micropotential being zero means one of the material points is not within the horizon of the other material point. As shown in Fig. 2, although the material point with a blue (smaller) horizon is inside the horizon of the material point with red (larger) horizon, the material point with a red horizon is outside of the horizon of the material point with a blue horizon.

For non-ordinary state-based peridynamics, peridynamic forces for variable horizon can be expressed as

$$\mathbf{t}_{kj} = \alpha_{kj} \left\{ \mathbf{P}\left[\mathbf{x}_k\right] \mathbf{K}^{-1}\left[\mathbf{x}_k\right] \left(\mathbf{x}_j - \mathbf{x}_k\right) \right\} \tag{18}$$

$$\mathbf{t}_{jk} = \alpha_{jk} \left\{ \mathbf{P}\left[\mathbf{x}_j\right] \mathbf{K}^{-1}\left[\mathbf{x}_j\right] \left(\mathbf{x}_k - \mathbf{x}_j\right) \right\} \tag{19}$$

where $\mathbf{P}$ is the first Piola–Kirchhoff stress tensor. The shape tensor, $\mathbf{K}$, for the material points k and j is defined as

$$\mathbf{K}\left[\mathbf{x}_k\right] = \sum_{i=1}^{N_k} \left(\mathbf{x}_i - \mathbf{x}_k\right) \otimes \left(\mathbf{x}_i - \mathbf{x}_k\right) V_i \tag{20}$$

$$\mathbf{K}\left[\mathbf{x}_j\right] = \sum_{i=1}^{N_j} \left(\mathbf{x}_i - \mathbf{x}_j\right) \otimes \left(\mathbf{x}_i - \mathbf{x}_j\right) V_i \tag{21}$$

where the symbol $\otimes$ represents the dyadic product. Note that non-ordinary state-based formulation can suffer from the zero-energy mode problem. In this study, the zero-energy mode problem is prevented by following the approach given in Silling [47].

For bond-based peridynamics, peridynamic force between two interacting material points is only influenced by the motion of these two material points. In other words, only micropotentials which belong to both interacting points exist, i.e. $\omega_{ik} = \omega_{ki} = 0$, if $i \neq j$. Therefore, peridynamic forces given in Eqs. (6) and (7) can be simplified as

$$\mathbf{t}_{kj} = \frac{1}{2}\left(\frac{\partial \omega_{kj}}{\partial \left(\mathbf{y}_j - \mathbf{y}_k\right)}\right) \tag{22}$$

$$\mathbf{t}_{jk} = \frac{1}{2}\left(\frac{\partial \omega_{jk}}{\partial \left(\mathbf{y}_k - \mathbf{y}_j\right)}\right). \tag{23}$$

These forces can also be expressed as

$$\mathbf{t}_{kj} = \alpha_{kj}\left(\frac{c}{2}s_{kj}\right)\frac{\mathbf{y}_j - \mathbf{y}_k}{\left|\mathbf{y}_j - \mathbf{y}_k\right|} \tag{24}$$

$$\mathbf{t}_{jk} = \alpha_{jk}\left(\frac{c}{2}s_{kj}\right)\frac{\mathbf{y}_k - \mathbf{y}_j}{\left|\mathbf{y}_k - \mathbf{y}_j\right|} \tag{25}$$

where c is the bond constant which can be written for an isotropic material and two-dimensional domain as

$$c = \frac{9E}{\pi h \delta^3} \tag{26}$$

with E being the elastic modulus.

3 Boundary condition

Since PD equations are in the form of integro-differential equations, the way to apply boundary conditions in PD is different than CCM. Boundary conditions in PD are applied through volumes, and these volumes are sometimes created as fictitious regions outside the actual solution domain. In this study, boundary volumes are chosen as fictitious regions, $\Re_f$, outside of the main solution domain, $\Re$, as shown in Fig. 3, which is an effective procedure suggested in [14].

3.1 Displacement constraints

In this study, the size of the fictitious region is specified as twice the horizon size, i.e. 2δ, and only two-dimensional problems are considered. However, the presented approach can be easily extended to three-dimensional models. The prescribed boundary value of the displacements U^* and V^* in the $x-$ and $y-$ directions can be applied by specifying the displacements of the material points in the fictitious region, u_f and v_f, in terms of displacements of the material points in the actual domain, u and v, as (Fig. 3)

$$u_f\left(x_f, y_f, t + \Delta t\right) = 2U^*\left(x^*, y^*, t + \Delta t\right) - u\left(x, y, t\right) \tag{27}$$

$$v_f\left(x_f, y_f, t + \Delta t\right) = 2V^*\left(x^*, y^*, t + \Delta t\right) - v\left(x, y, t\right). \tag{28}$$
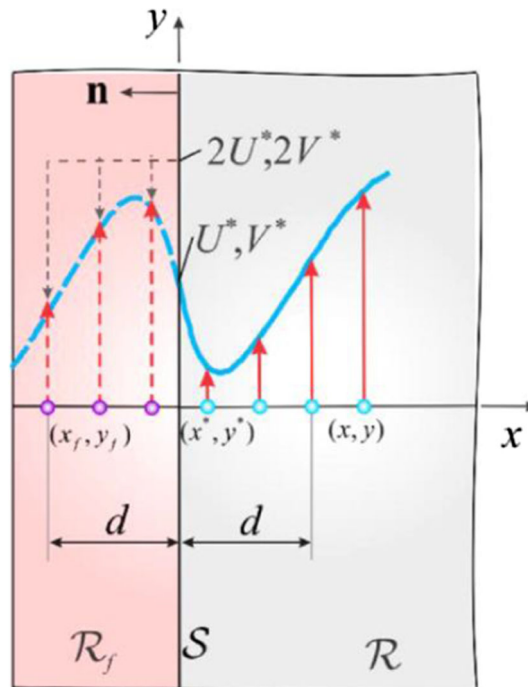
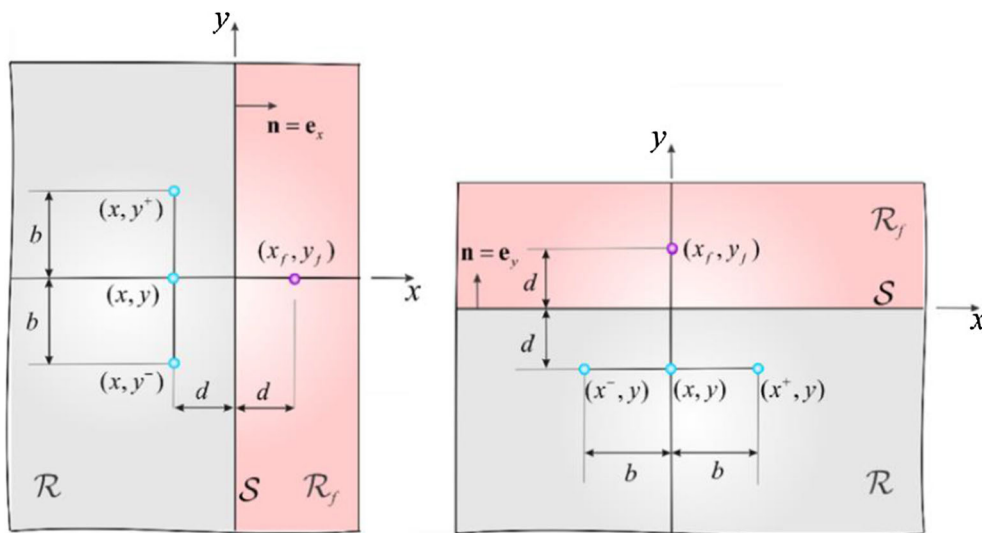**Fig. 3** Application of displacement constraints in PD introducing a fictitious region [14]

Fig. 4 Application of traction boundary conditions on a surface with a normal vector **(a)** in the x-direction and **(b)** in the y-direction in PD introducing a fictitious region [14]

3.2 Traction boundary conditions

Traction boundary conditions can also be applied similar to displacement constraints by using a fictitious region as shown in Fig. 4. The displacements of the material points in the fictitious region depend on the unit normal of the boundary on which the traction boundary condition, σ_{ij}^*, with $i, j = x, y$, is exerted.
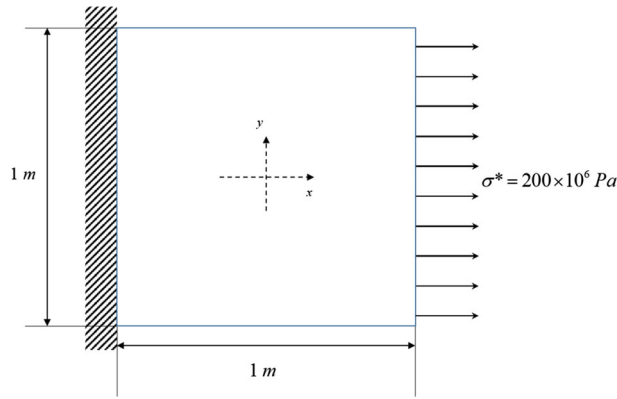
Fig. 5 Square plate subjected to uniaxial tension loading
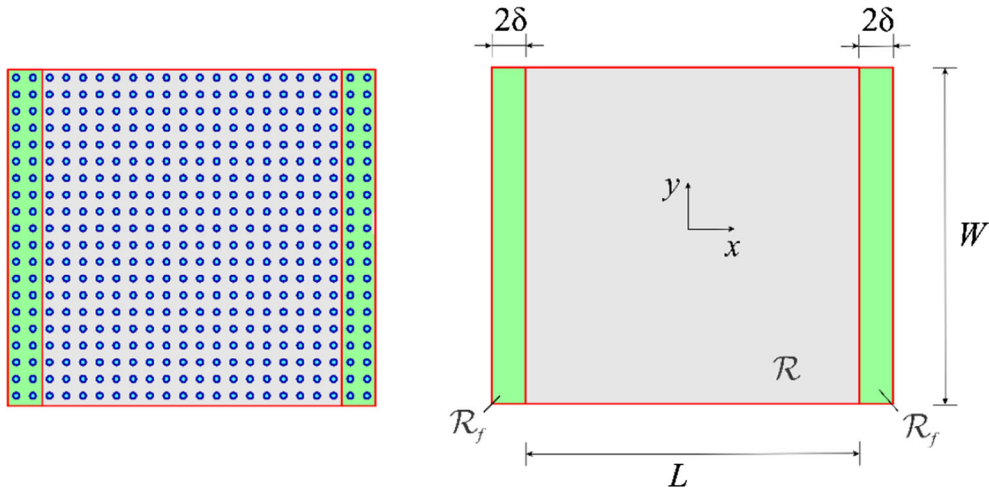
Fig. 6 Geometry and discretisation of the square plate

For the traction boundary with a unit normal in the $x-$direction, they can be written as [14]

$$u_f\left(x_f, y_f, t + \Delta t\right) = \left[\frac{\sigma_{xx}^* \left(1 - v^2\right)}{E} - v \frac{v\left(x, y^+, t\right) - v\left(x, y^-, t\right)}{y^+ - y^-}\right]\left(x_f - x\right) + u\left(x, y, t\right) \quad (29)$$

$$v_f\left(x_f, y_f, t + \Delta t\right) = \left[\frac{2\left(1 + v\right)\sigma_{xy}^*}{E} - \frac{u\left(x, y^+, t\right) - u\left(x, y^-, t\right)}{y^+ - y^-}\right]\left(x_f - x\right) + v\left(x, y, t\right). \quad (30)$$

Similarly, for the traction boundary with a unit normal in the $y-$direction, they can be written as

$$u_f\left(x_f, y_f, t + \Delta t\right) = \left[\frac{2\left(1 + v\right)\sigma_{xy}^*}{E} - \frac{v\left(x^+, y, t\right) - v\left(x^-, y, t\right)}{x^+ - x^-}\right]\left(y_f - y\right) + u\left(x, y, t\right) \quad (31)$$

$$v_f\left(x_f, y_f, t + \Delta t\right) = \left[\frac{\sigma_{yy}^* \left(1 - v^2\right)}{E} - v\frac{u\left(x^+, y, t\right) - v\left(x^-, y, t\right)}{x^+ - x^-}\right]\left(y_f - y\right) + v\left(x, y, t\right). \quad (32)$$

4 Surface correction

Determination of surface correction factors for ordinary state-based peridynamics is important not only for material points close to the surfaces due to lack of interactions, but also for material points inside the solution
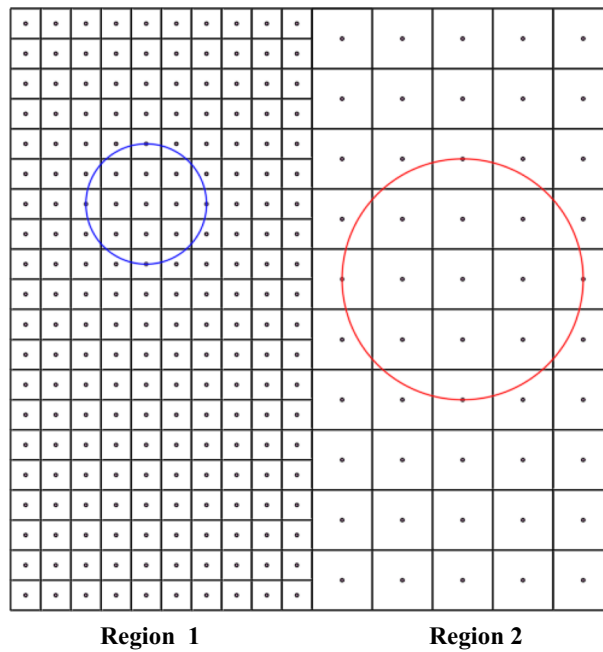
Fig. 7 Discretisation and horizons for refined grid–coarse grid case
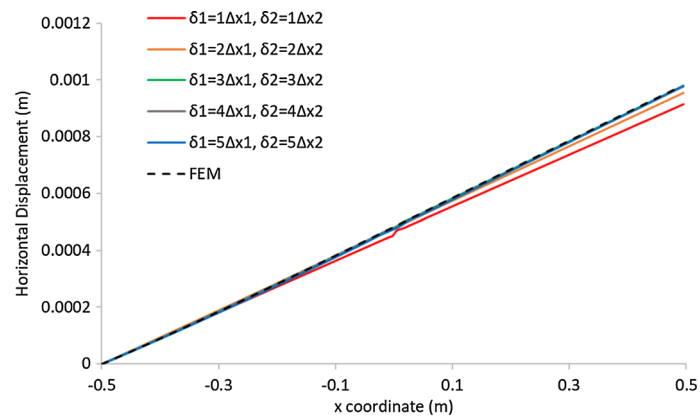
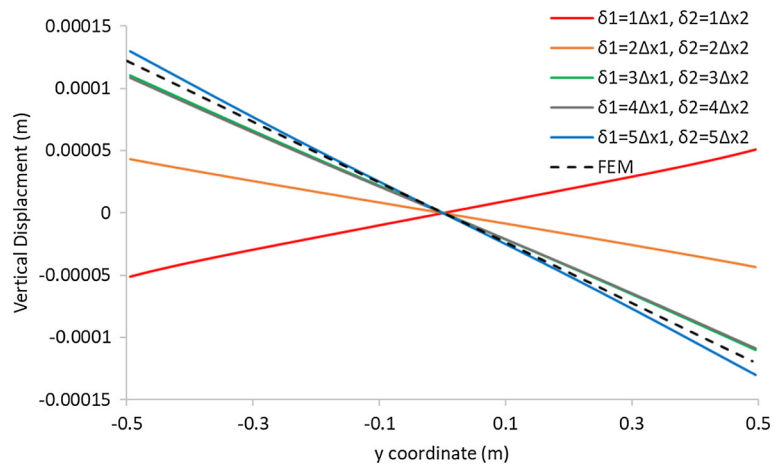**Fig. 8** Variation of horizontal displacements along the central axis $(x, y = 0)$

Fig. 9 Variation of vertical displacement along the central axis $(x = 0, y)$
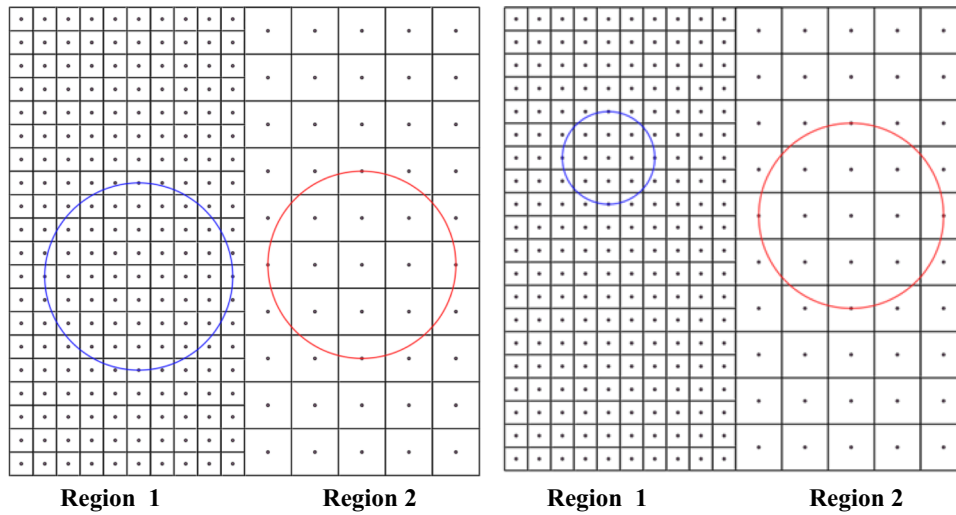
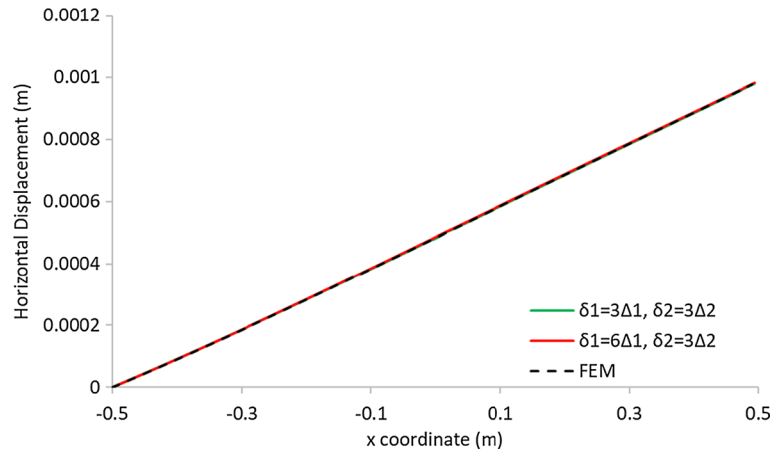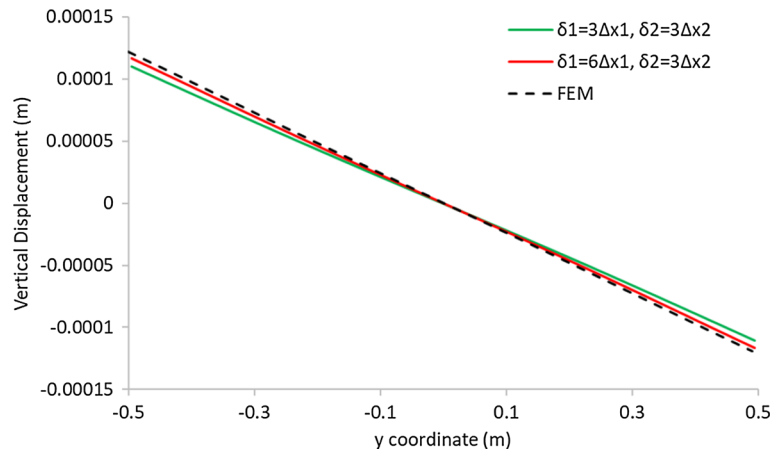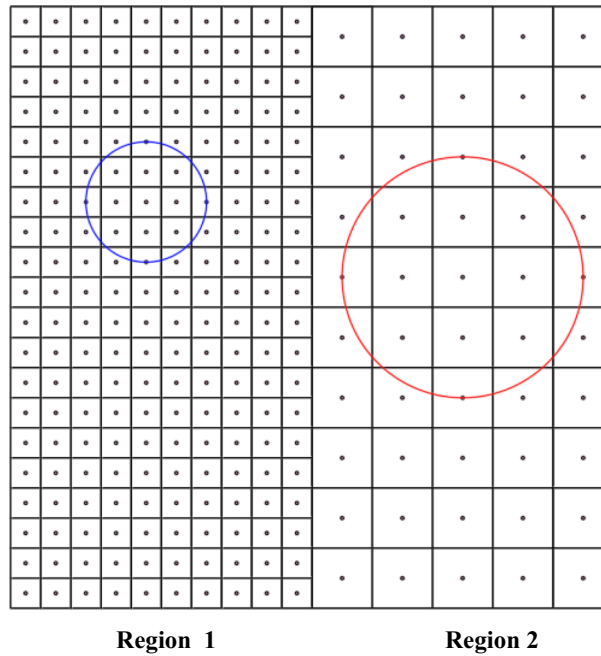**Fig. 10** Discretisation and horizons for refined grid–coarse grid case

Fig. 11 Variation of horizontal displacements along the central axis $(x, y = 0)$

Fig. 12 Variation of vertical displacements along the central axis $(x = 0, y)$

Fig. 13 Discretisation and horizons for refined grid–coarse grid case

domain since spatial numerical integration scheme based on meshless approach introduces numerical error to the solution. These errors can be corrected by using surface correction factors and modifying the peridynamic dilatation terms and peridynamic force expressions given in Eqs. (8,9,13,14) as

$$\theta_k = \sum_{i=1}^{N_k} \beta_k d \delta_k s_{ki} V_i \tag{33}$$

$$\theta_j = \sum_{i=1}^{N_j} \beta_j d \delta_j s_{ji} V_i \tag{34}$$

and

$$\mathbf{t}_{kj} = \alpha_{kj} \left(\frac{2ad\delta_k}{|\mathbf{x}_j - \mathbf{x}_k|} \theta_k (\mathbf{x}_k, t) + \lambda_k b \, s_{kj} \right) \frac{\mathbf{y}_j - \mathbf{y}_k}{|\mathbf{y}_j - \mathbf{y}_k|} \tag{35}$$

$$\mathbf{t}_{jk} = \alpha_{jk} \left(\frac{2ad\delta_j}{|\mathbf{x}_j - \mathbf{x}_k|} \theta_j (\mathbf{x}_j, t) + \lambda_j b s_{kj} \right) \frac{\mathbf{y}_k - \mathbf{y}_j}{|\mathbf{y}_k - \mathbf{y}_j|} \tag{36}$$

where β and λ represent the surface correction terms for the dilatation and peridynamic force expressions, respectively. As explained in Madenci and Oterkus [4], surface correction factors can be obtained by considering a simple loading condition and determining the ratio of the dilatation and strain energy density of a particular material point calculated from CCM and PD. Note that surface correction factors are not necessary for the non-ordinary state-based formulation since correction is automatically done within the formulation.

5 Numerical results

As mentioned earlier, although uniform discretisation is widely used in the peridynamic studies available in the scientific literature, it can be computationally advantageous to have flexibility to use different grid sizes at different parts of the solution domain which is a common procedure used in other numerical methods such as finite element method (FEM). Hence, in this section, we present the capability of dual-horizon peridynamics
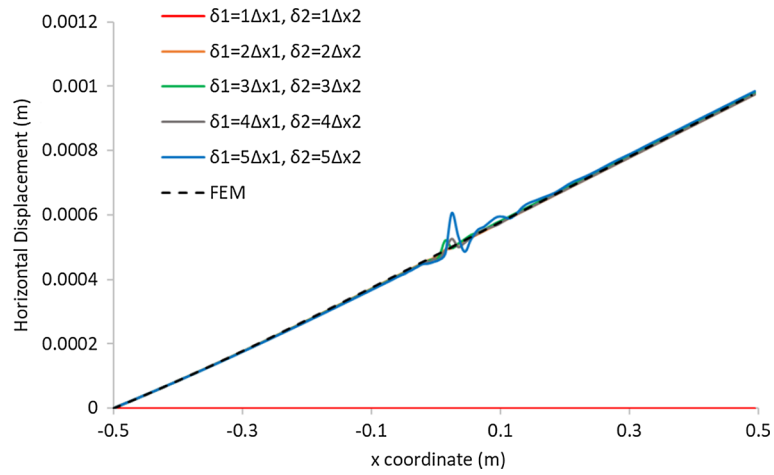
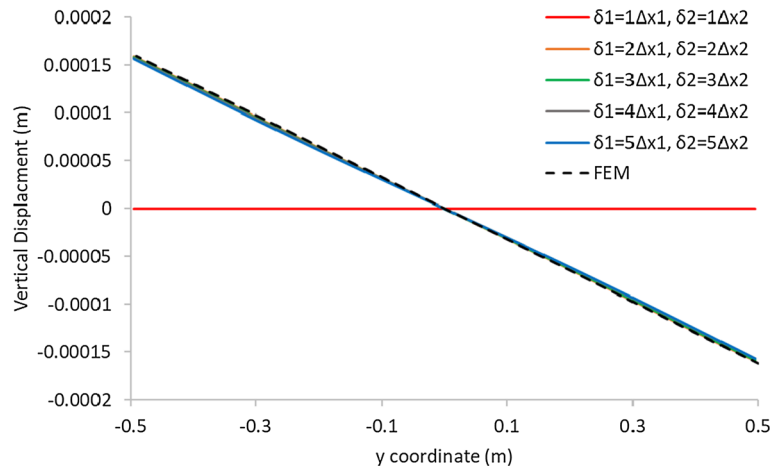**Fig. 14** Variation of horizontal displacements along the central axis $(x, y = 0)$

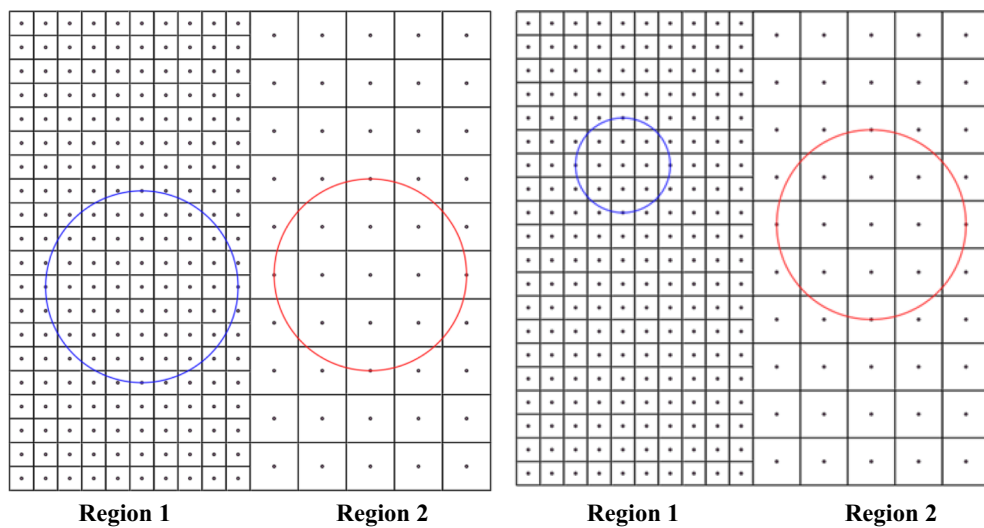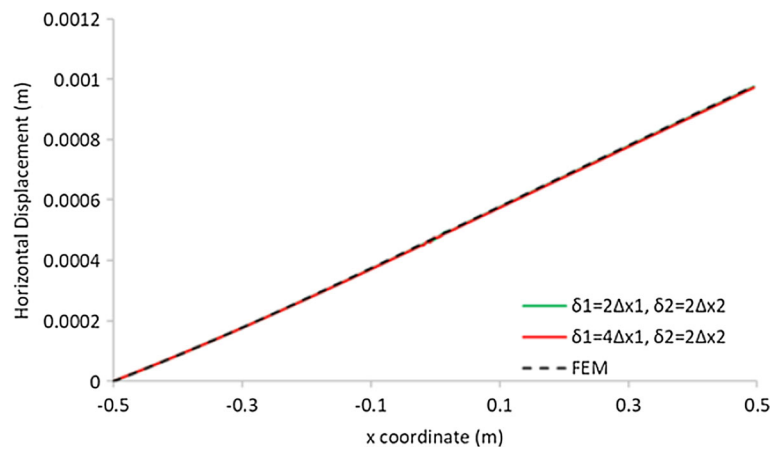**Fig. 15** Variation of vertical displacements along the central axis $(x = 0, y)$

Region 1   Region 2   Region 1   Region 2

Fig. 16 Discretisation and horizons for refined grid–coarse grid case

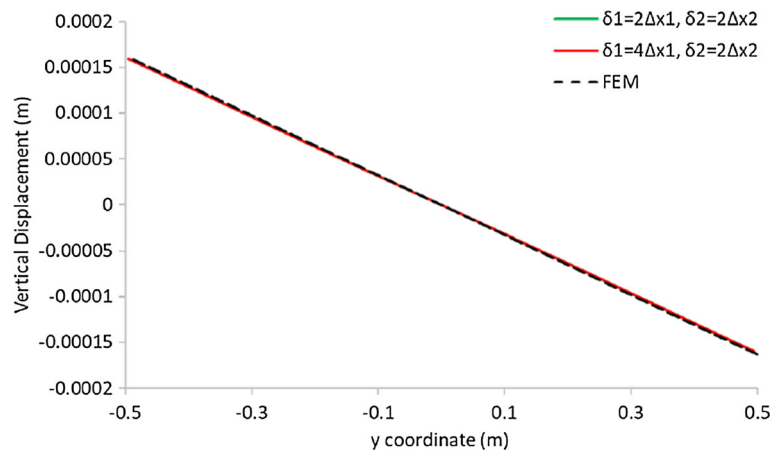**Fig. 17** Variation of horizontal displacements along the central axis $(x, y = 0)$

Fig. 18 Variation of vertical displacements along the central axis $(x = 0, y)$
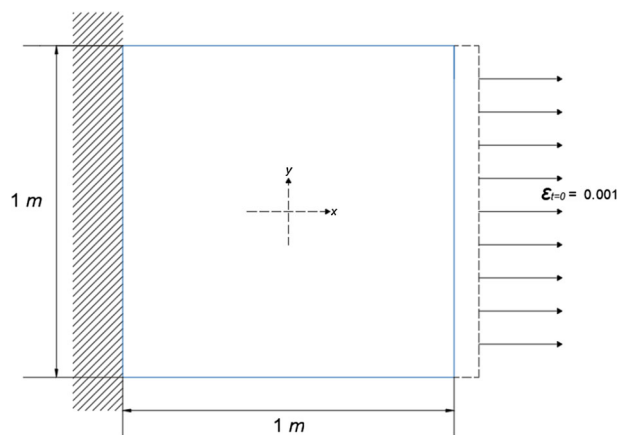

Fig. 19 Square plate subjected to initial uniaxial strain condition

using variable grid sizes and horizons based on the formulation given in Sects. 2, 3 and 4. The solution domain is split into two regions so that each of these regions can have different grid sizes and horizon sizes. In the first problem case, plate under tension problem is considered in Sect. 5.1 to validate the dual-horizon peridynamic formulation for static problems. As the second validation case, vibration of a plate problem considered in Sect. 5.2 is investigated to validate the dual-horizon peridynamic formulation for dynamic problems.
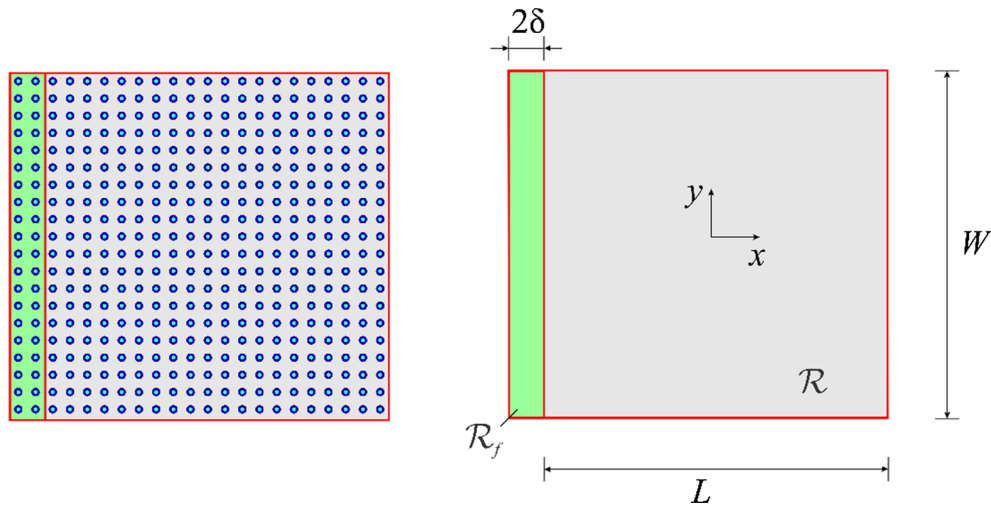
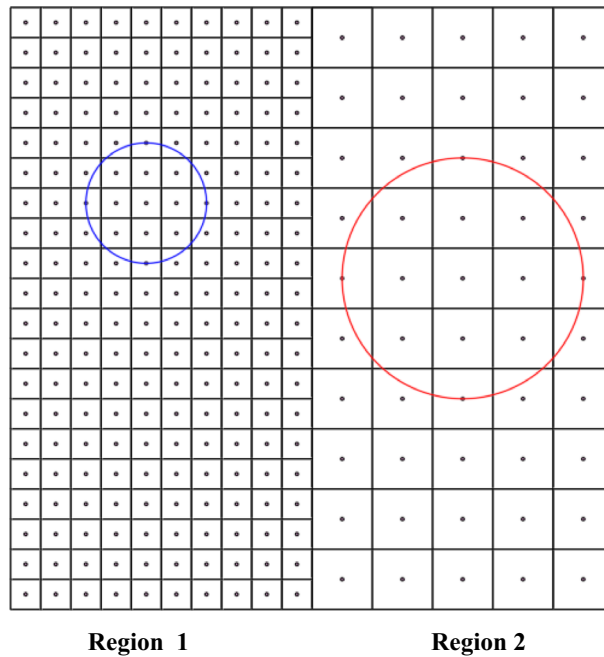**Fig. 20** Geometry and discretisation of the square plate

Fig. 21 Discretisation and horizons for refined grid–coarse grid case

5.1 Plate under tension

In the first problem case, a square plate with dimensions of $L = W = 1$m is considered. The plate has a thickness of 0.01 m and subjected to a uniaxial tension loading of $\sigma* = 200$ MPa at the right edge as shown in Fig. 5. The applied loading is specified by creating a fictitious region at the right edge as demonstrated in Fig. 6. Elastic modulus and density of the plate are specified as 200 GPa and 7850 kg/m^3, respectively. The left edge of the plate is fully fixed by using a fictitious region (Fig. 6). The steady-state solution is obtained by utilising the adaptive dynamic relaxation technique [48].

5.1.1 Ordinary state-based peridynamics

A plate under tension is first analysed by using ordinary state-based peridynamics. The solution domain is split into two equal regions as Region 1 and Region 2 as shown in Fig. 7. The discretisation size in Region 1,
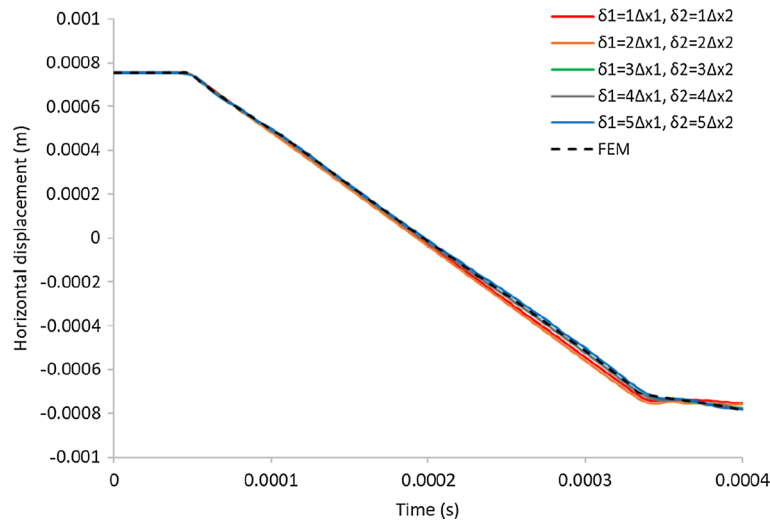
Fig. 22 Variation of horizontal displacement of the material point located at (0.255 m, 0.255 m) with time
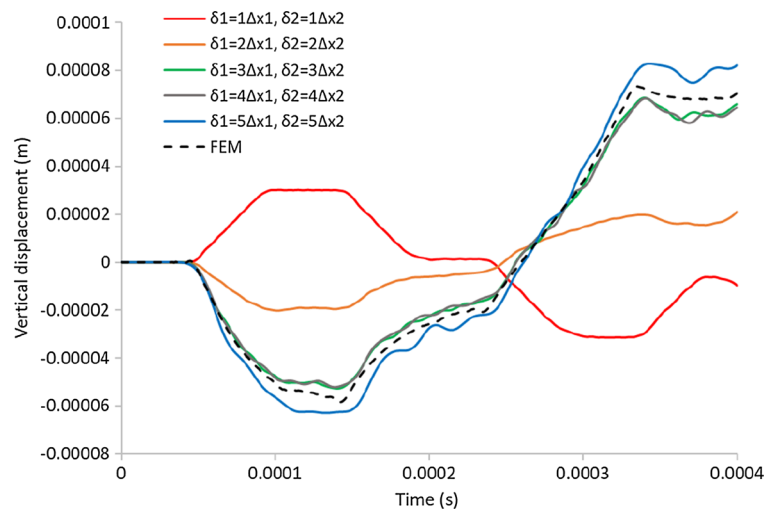

Fig. 23 Variation of vertical displacement of the material point located at (0.255 m, 0.255 m) with time

$\Delta x_1 = 0.005$ m, is half of the discretisation size of Region 2, $\Delta x_2 = 0.01$ m. Material points in both regions are interacting with the same number of material points. This also means that the horizon size of material points in Region 1, δ_1, is half of the horizon size in Region 2, δ_2. Note that dual-horizon peridynamics formulation is especially effective for the material points close to the interface of Regions 1 and 2 since material points in one of these regions are interacting with material points in the other region.

Five different horizon size values are considered, i.e. $\delta_1 = n\Delta x_1$, $\delta_2 = n\Delta x_2$, $n = 1,...5$. Variation of horizontal displacements along the central axes is shown in Figs. 8 and 9. The horizon size values of $\delta_1 = 3\Delta x_1$ & $\delta_2 = 3\Delta x_2$, $\delta_1 = 4\Delta x_1$ & $\delta_2 = 4\Delta x_2$ and $\delta_1 = 5\Delta x_1$ & $\delta_2 = 5\Delta x_2$ have better agreement with FEM results obtained by using ANSYS, a commercial finite element software.

In addition, the effect of the horizon size is investigated by considering the same horizon sizes for Regions 1 and 2 as shown in Fig. 10, i.e. $\delta_1 = \delta_2 = 6\Delta x_1 = 3\Delta x_2$, and compared against the different horizon case considered earlier with the horizon size in Region 1, $\delta_1 = 3\Delta x_1$, and the horizon size in Region 2, $\delta_2 = 3\Delta x_2$. As shown in Figs. 11 and 12, although both cases provide good agreement with FEM results for horizontal displacements, equal horizon case yields better vertical displacement results with respect to FEM results since there are more material points inside the horizon in Region 1 for this case.
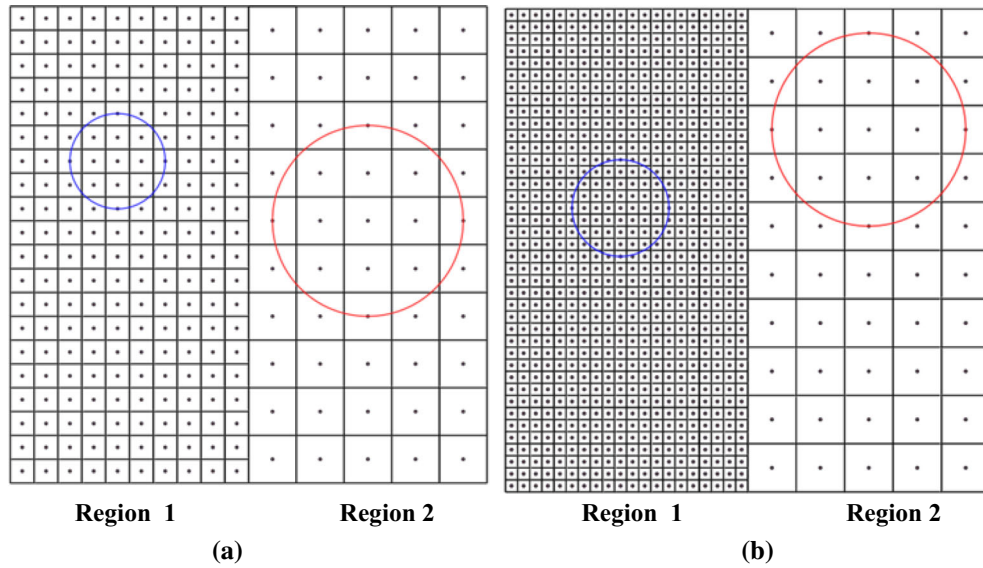
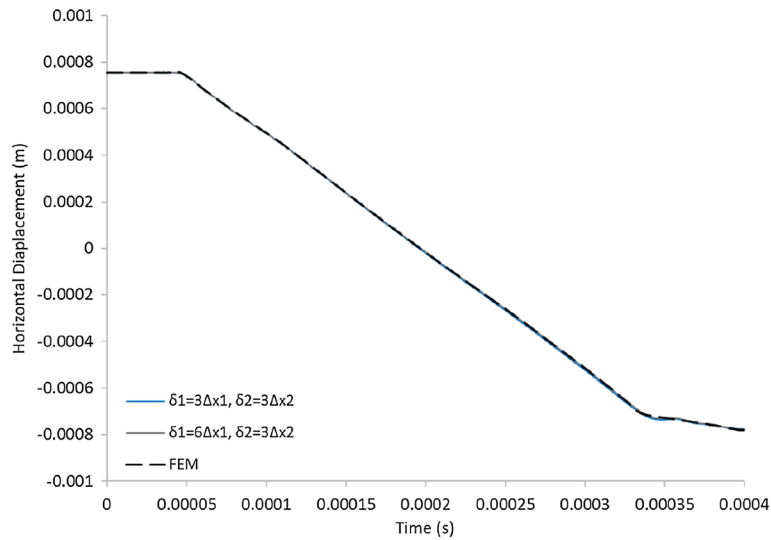**Fig. 24** Discretisation and horizons for **a** Case 1 and **b** Case 2

Fig. 25 Variation of horizontal displacement of the material point located at (0.255 m, 0.255 m) with time

5.1.2 Non-ordinary state-based peridynamics

In this section, a plate under tension problem is analysed by using non-ordinary state-based peridynamics. As in the previous section, the horizon size and discretisation size of Region 1 are half of the Region 2 (Fig. 13). Five different horizon size cases are considered, i.e. $\delta_1 = n\Delta x_1$, $\delta_2 = n\Delta x_2$, $n = 1,\dots5$, and the variation of horizontal and vertical displacements along the central axes is shown in Figs. 14 and 15. According to these figures, the horizon size value of $\delta_1 = 2\Delta x_1$ & $\delta_2 = 2\Delta x_2$ has better agreement with FEM results since it provides smoother transition between the two regions which is a different outcome than ordinary state-based case. As the horizon size increases, error at the interface region increases.

Next, equal size horizon for both Regions 1 and 2 is considered and compared against the case with different horizon sizes in Regions 1 and 2 where the horizon size in Region 1, $\delta_1 = 2\Delta x_1$, is half of the horizon size in Region 2, $\delta_2 = 2\Delta x_2$ (Fig. 16). As shown in Figs. 17 and 18, both cases yield good agreement with FEM results.
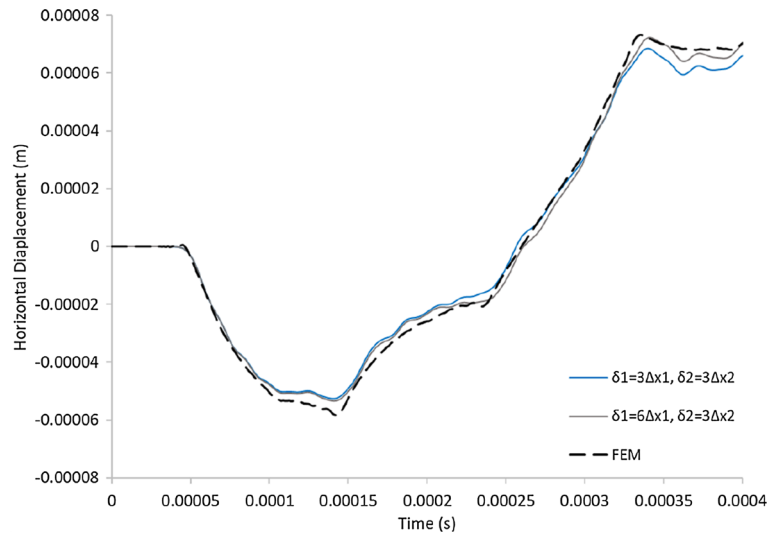
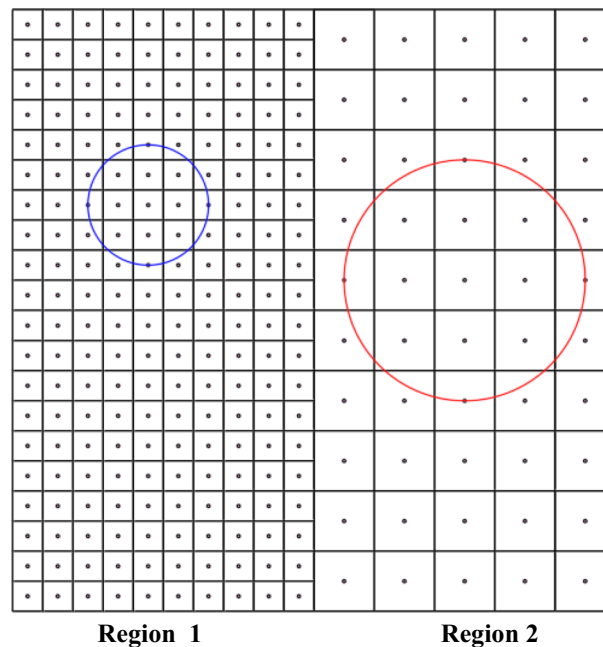**Fig. 26** Variation of vertical displacement of the material point located at (0.255 m, 0.255 m) with time

Fig. 27 Discretisation and horizons for refined grid–coarse grid case

5.2 Vibration of a plate

In the second problem case, the square plate considered in the previous case is subjected to an initial condition in the form of uniaxial strain of 0.001 in the x-direction as shown in Fig. 19. The solution is obtained using explicit time integration [4] with a time step size of 1×10^{-7} s (Fig. 20).

5.2.1 Ordinary state-based peridynamics

As in the plate under tension problem, first solution is obtained by using ordinary state-based peridynamics. The solution domain is split into two equal regions as Region 1 and Region 2 as shown in Fig. 21. The discretisation size in Region 1, $\Delta x_1 = 0.005$ m, is half of the discretisation size of Region 2, $\Delta x_2 = 0.01$ m. Moreover, the horizon size of material points in Region 1, δ_1, is half of the horizon size in Region 2, δ_2.
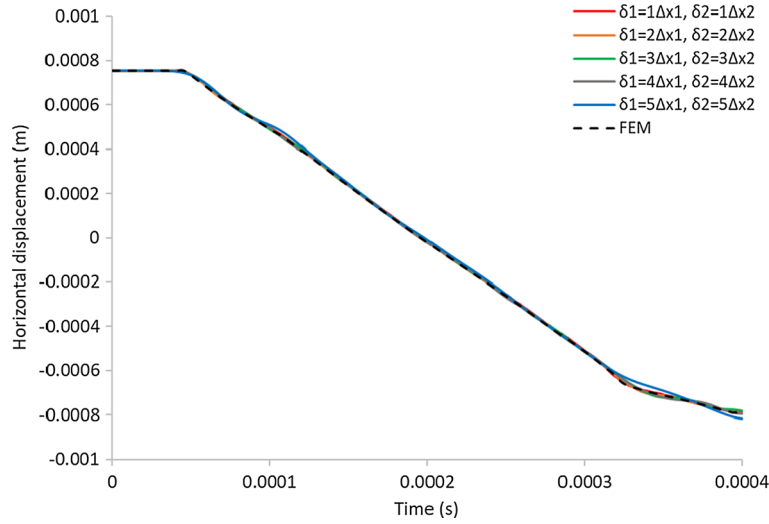
Fig. 28 Variation of horizontal displacement of the material point located at (0.255 m, 0.255 m) with time
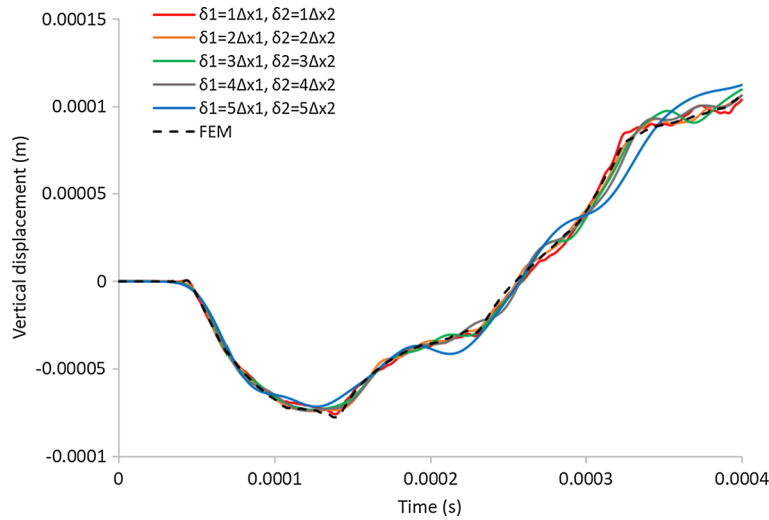

Fig. 29 Variation of horizontal displacement of the material point located at (0.255 m, 0.255 m) with time

Five different horizon size values are considered, $\delta_1 = n\Delta x_1$, $\delta_2 = n\Delta x_2$, $n =1,...5$. To analyse the results, a suitable point which is located far from the surfaces and the central axes is selected which is located at (0.255 m, 0.255 m). The variation of horizontal and vertical displacements at this point as the time progresses is shown in Figs. 22 and 23 for five different horizon size values. According to these results, the horizon size values of $\delta_1 = 3\Delta x_1$ & $\delta_2 = 3\Delta x_2$ and $\delta_1 = 4\Delta x_1$ & $\delta_2 = 4\Delta x_2$ provide better agreement with FEM results.

Next, the effect of discretisation size is investigated. By keeping the same horizon sizes as before, the discretisation size in Region 1 is specified as half of the previous case as shown in Fig. 24. Therefore, the grid size in Region 2 is $\Delta x_2 = 0.01$, whereas the grid size in Region 1 is $\Delta x_1 = 0.005$ for Case 1 and $\Delta x_1 = 0.025$ for Case 2. The horizon size in Region 1 is half of the horizon size in Region 2, $\delta_2 = 3\Delta x_2$. As shown in Figs. 25 and 26, although horizontal displacements in both cases are similar to each other, Case 2 yields better vertical displacement results with respect to Case 1 since there are more material points inside the horizon of Region 1 in Case 2.

5.2.2 Non-ordinary state-based peridynamics

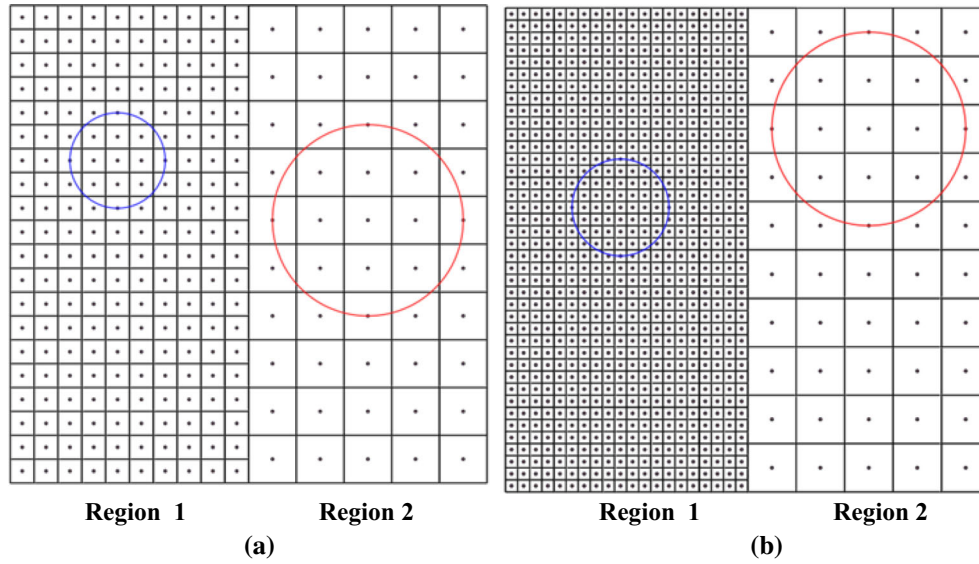Finally, the vibration of a plate problem is analysed by using non-ordinary state-based peridynamics.

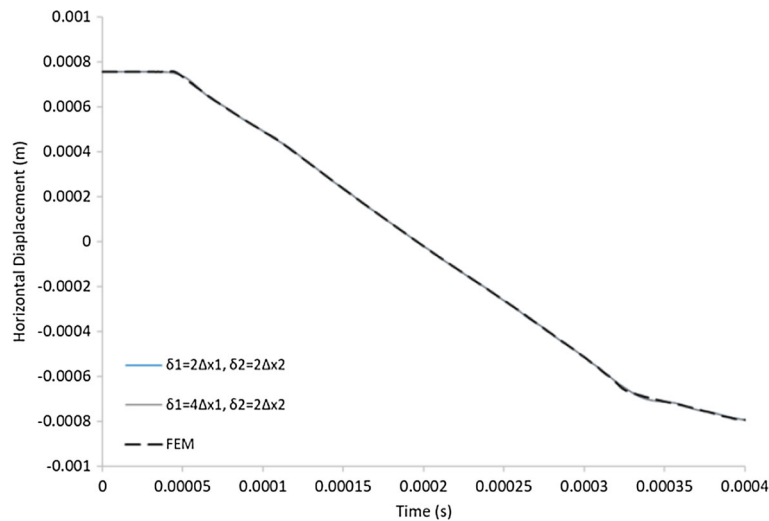**Fig. 30** Discretisation and horizons for **a** Case 1 and **b** Case 2

Fig. 31 Variation of horizontal displacement of the material point located at (0.255 m, 0.255 m) with time

Five different horizon sizes are considered, $\delta_1 = n\Delta x_1$, $\delta_2 = n\Delta x_2$, $n =1,\dots5$. The horizon size in Region 1 is half of the horizon size in Region 2 (Fig. 27). As shown in Figs. 28 and 29, the horizon size value of $\delta_1 = 2\Delta x_1$ & $\delta_2 = 2\Delta x_2$ has better agreement with FEM results.

Next, two different non-uniform discretisation cases are compared (Fig. 30). The grid size in Region 2 is $\Delta x_2 = 0.01$, whereas the grid size in Region 2 is $\Delta x_1 = 0.005$ for Case 1 and $\Delta x_1 = 0.025$ for Case 2. The horizon size in Region 1 is half of the horizon size in Region 2, $\delta_2 = 2\Delta x_2$. As shown in Figs. 31 and 32, both cases provide similar results and good agreement with FEM solution.
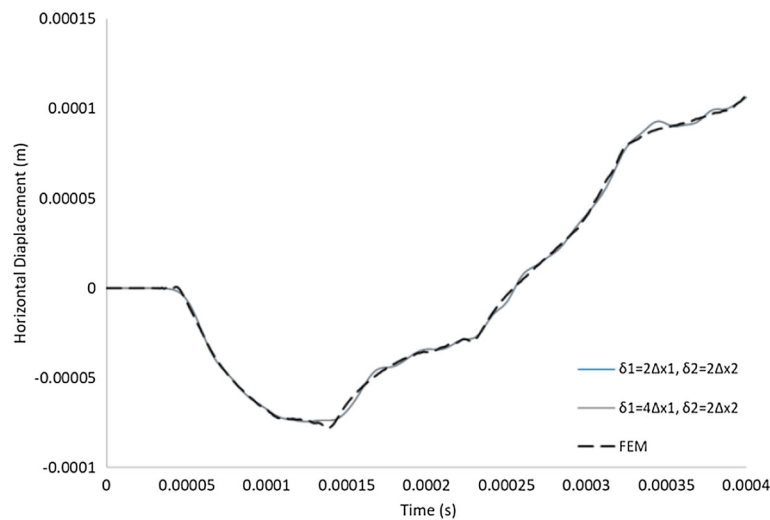
Fig. 32 Variation of horizontal displacement of the material point located at (0.255 m, 0.255 m) with time

6 Conclusions

In this study, dual-horizon peridynamics formulation was derived by using Euler–Lagrange equation. Dual-horizon peridynamics is an effective methodology when non-uniform discretisation and variable horizon sizes are considered either due to computational efficiency purposes and/or due to physical requirement of the problem. After deriving the dual-horizon peridynamic formulation for both ordinary and non-ordinary state-based peridynamics, two benchmark problems were analysed to investigate the effect of discretisation size and horizon size. By comparing PD results against FEM results, non-ordinary state-based peridynamics provides better agreement for smaller horizons sizes and error at the interface becomes larger as the horizon size increases. On the other hand, for ordinary state-based peridynamics results, the results at the interface are smoother and the results are getting better as the horizon size increases. Moreover, as the number of points inside the horizon is increasing, a better agreement is obtained for a constant horizon size in the solution domain. Finally, with the advancement of additive manufacturing technologies, fabrication of complex materials such as microstructured materials is possible. PD theory can be a suitable alternative for the analysis of microstructured materials to some other approaches presented in the literature [49–51], especially for damage prediction.

References

1. Silling, S.A.: Reformulation of elasticity theory for discontinuities and long-range forces. J. Mech. Phys. Solids **48**(1), 175–209 (2000)
2. dell'Isola, F., Andreaus, U., Placidi, L.: At the origins and in the vanguard of peridynamics, non-local and higher-gradient continuum mechanics: an underestimated and still topical contribution of Gabrio Piola. Math. Mech. Solids **20**(8), 887–928 (2015)
3. dell'Isola, F., Della Corte, A., Esposito, R. and Russo, L.: Some cases of unrecognized transmission of scientific knowledge: from antiquity to Gabrio Piola's peridynamics and generalized continuum theories. In: Generalized Continua as Models for Classical and Advanced Materials (pp. 77–128). Springer, Cham (2016)
4. Madenci, E., Oterkus, E.: Peridynamic Theory and its Applications, vol. 17. Springer, New York (2014)

5. Oterkus, E., Barut, A., Madenci, E.: Damage growth prediction from loaded composite fastener holes by using peridynamic theory. In: 51st AIAA/ASME/ASCE/AHS/ASC Structures, Structural Dynamics, and Materials Conference 18th AIAA/ASME/AHS Adaptive Structures Conference 12th (p. 3026) (2010)
6. Oterkus, E., Madenci, E.: Peridynamics for failure prediction in composites. In: 53rd AIAA/ASME/ASCE/AHS/ASC Structures, Structural Dynamics and Materials Conference 20th AIAA/ASME/AHS Adaptive Structures Conference 14th AIAA (p. 1692) (2012)
7. Oterkus, E., Madenci, E.: Peridynamic theory for damage initiation and growth in composite laminate. Key Eng. Mater. **488**, 355–358 (2012)
8. De Meo, D., Zhu, N., Oterkus, E.: Peridynamic modeling of granular fracture in polycrystalline materials. J. Eng. Mater. Technol. **138**(4), 041008 (2016)
9. Zhu, N., De Meo, D., Oterkus, E.: Modelling of granular fracture in polycrystalline materials using ordinary state-based peridynamics. Materials **9**(12), 977 (2016)
10. Lu, W., Li, M., Vazic, B., Oterkus, S., Oterkus, E., Wang, Q.: Peridynamic modelling of fracture in polycrystalline ice. J. Mech. **36**(2), 223–234 (2020)
11. Oterkus, E., Guven, I., Madenci, E.: Impact damage assessment by using peridynamic theory. Open Eng. **2**(4), 523–531 (2012)
12. Guski, V., Verestek, W., Oterkus, E., Schmauder, S.: Microstructural investigation of plasma sprayed ceramic coatings using peridynamics. J. Mech. **36**(2), 183–196 (2020)
13. Vazic, B., Oterkus, E., Oterkus, S.: In-plane and out-of plane failure of an ice sheet using peridynamics. J. Mech. **36**(2), 265–271 (2020)
14. Liu, X., He, X., Wang, J., Sun, L., Oterkus, E.: An ordinary state-based peridynamic model for the fracture of zigzag graphene sheets. Proc. R. Soc. A Math. Phys. Eng. Sci. **474**(2217), 20180019 (2018)
15. Oterkus, E., Guven, I., Madenci, E.: Fatigue failure model with peridynamic theory. In: 2010 12th IEEE Intersociety Conference on Thermal and Thermomechanical Phenomena in Electronic Systems (pp. 1–6). IEEE (2010)
16. Madenci, E., Oterkus, S.: Ordinary state-based peridynamics for plastic deformation according to von Mises yield criteria with isotropic hardening. J. Mech. Phys. Solids **86**, 192–219 (2016)
17. Madenci, E., Oterkus, S.: Ordinary state-based peridynamics for thermoviscoelastic deformation. Eng. Fract. Mech. **175**, 31–45 (2017)
18. Amani, J., Oterkus, E., Areias, P., Zi, G., Nguyen-Thoi, T., Rabczuk, T.: A non-ordinary state-based peridynamics formulation for thermoplastic fracture. Int. J. Impact Eng **87**, 83–94 (2016)
19. Gao, Y., Oterkus, S.: Ordinary state-based peridynamic modelling for fully coupled thermoelastic problems. Continuum Mech. Thermodyn. **31**(4), 907–937 (2019)
20. Alpay, S., Madenci, E.: Crack growth prediction in fully-coupled thermal and deformation fields using peridynamic theory. In: 54th AIAA/ASME/ASCE/AHS/ASC Structures, Structural Dynamics, and Materials Conference (p. 1477) (2013)
21. Oterkus, S., Fox, J., Madenci, E.: Simulation of electro-migration through peridynamics. In: 2013 IEEE 63rd Electronic Components and Technology Conference (pp. 1488–1493). IEEE (2013)
22. Wang, H., Oterkus, E., Oterkus, S.: Predicting fracture evolution during lithiation process using peridynamics. Eng. Fract. Mech. **192**, 176–191 (2018)
23. De Meo, D., Oterkus, E.: Finite element implementation of a peridynamic pitting corrosion damage model. Ocean Eng. **135**, 76–83 (2017)
24. Diyaroglu, C., Oterkus, S., Oterkus, E., Madenci, E., Han, S., Hwang, Y.: Peridynamic wetness approach for moisture concentration analysis in electronic packages. Microelectron. Reliab. **70**, 103–111 (2017)
25. Oterkus, S., Madenci, E., Oterkus, E., Hwang, Y., Bae, J., Han, S.: Hygro-thermo-mechanical analysis and failure prediction in electronic packages by using peridynamics. In: 2014 IEEE 64th Electronic Components and Technology Conference (ECTC) (pp. 973–982). IEEE (2014)
26. Oterkus, S., Madenci, E., Oterkus, E.: Fully coupled poroelastic peridynamic formulation for fluid-filled fractures. Eng. Geol. **225**, 19–28 (2017)
27. Gao, Y., Oterkus, S.: Non-local modeling for fluid flow coupled with heat transfer by using peridynamic differential operator. Eng. Anal. Boundary Elem. **105**, 104–121 (2019)
28. Gao, Y., Oterkus, S.: Nonlocal numerical simulation of low Reynolds number laminar fluid motion by using peridynamic differential operator. Ocean Eng. **179**, 135–158 (2019)
29. Yang, Z., Oterkus, E., Nguyen, C.T., Oterkus, S.: Implementation of peridynamic beam and plate formulations in finite element framework. Continuum Mech. Thermodyn. **31**(1), 301–315 (2019)
30. Diyaroglu, C., Oterkus, E., Oterkus, S.: An Euler-Bernoulli beam formulation in an ordinary state-based peridynamic framework. Math. Mech. Solids **24**(2), 361–376 (2019)
31. Yang, Z., Vazic, B., Diyaroglu, C., Oterkus, E., Oterkus, S.: A Kirchhoff plate formulation in a state-based peridynamic framework. Math. Mech. Solids **25**(3), 727–738 (2020)
32. Chowdhury, S.R., Roy, P., Roy, D., Reddy, J.N.: A peridynamic theory for linear elastic shells. Int. J. Solids Struct. **84**, 110–132 (2016)
33. Maier, G., Perego, U., Andreaus, U., Esposito, R., Forest, S.: The Complete Works of Gabrio Piola: Volume I Commented English Translation-English and Italian Edition (2014)
34. dell'Isola, F., Andreaus, U., Cazzani, A., Esposito, R., Placidi, L., Perego U., Seppecher, P.: The Complete Works of Gabrio Piola: Volume II (2014)
35. dell'Isola, F., Corte, A.D., Giorgio, I.: Higher-gradient continua: the legacy of Piola, Mindlin, Sedov and Toupin and some future research perspectives. Math. Mech. Solids **22**(4), 852–872 (2017)
36. dell'Isola, F., Seppecher, P., Alibert, J.J., Lekszycki, T., Grygoruk, R., Pawlikowski, M., Gołaszewski, M.: Pantographic metamaterials: an example of mathematically driven design and of its technological challenges. Continuum Mech. Thermodyn. **31**(4), 851–884 (2019)

37. dell'Isola, F., Seppecher, P., Spagnuolo, M., Barchiesi, E., Hild, F., Lekszycki, T., Eugster, S.R.: Advances in pantographic structures: design, manufacturing, models, experiments and image analyses. Continuum Mech. Thermodyn. **31**(4), 1231–1282 (2019)
38. dell'Isola, F., Giorgio, I., Pawlikowski, M., Rizzi, N.L.: Large deformations of planar extensible beams and pantographic lattices: heuristic homogenization, experimental and numerical examples of equilibrium. Proc. R. Soc. A Math. Phys. Eng. Sci. **472**(2185), 20150790 (2016)
39. Rahali, Y., Giorgio, I., Ganghoffer, J.F., dell'Isola, F.: Homogenization à la Piola produces second gradient continuum models for linear pantographic lattices. Int. J. Eng. Sci. **97**, 148–172 (2015)
40. Giorgio, I., Harrison, P., dell'Isola, F., Alsayednoor, J., Turco, E.: Wrinkling in engineering fabrics: a comparison between two different comprehensive modelling approaches. Proc. R. Soc. A Math. Phys. Eng. Sci. **474**(2216), 20180063 (2018)
41. Turco, E., Giorgio, I., Misra, A., dell'Isola, F.: King post truss as a motif for internal structure of (meta) material with controlled elastic properties. R. Soc. Open Sci. **4**(10), 171153 (2017)
42. Yildizdag, M. E., Tran, C. A., Barchiesi, E., Spagnuolo, M., dell'Isola, F., Hild, F.: A multi-disciplinary approach for mechanical metamaterial synthesis: a hierarchical modular multiscale cellular structure paradigm. In: State of the Art and Future Trends in Material Modeling (pp. 485–505). Springer, Cham (2019)
43. Yildizdag, M.E., Barchiesi, E., Dell'Isola, F.: Three-point bending test of pantographic blocks: numerical and experimental investigation. Math. Mech. Solids (2020). https://doi.org/10.1177/1081286520916911
44. Berezovski, A., Yildizdag, M.E., Scerrato, D.: On the wave dispersion in microstructured solids. Continuum Mech. Thermodyn. **32**, 569–588 (2020)
45. Ren, H., Zhuang, X., Cai, Y., Rabczuk, T.: Dual-horizon peridynamics. Int. J. Numer. Meth. Eng. **108**(12), 1451–1476 (2016)
46. Ren, H., Zhuang, X., Rabczuk, T.: Dual-horizon peridynamics: a stable solution to varying horizons. Comput. Methods Appl. Mech. Eng. **318**, 762–782 (2017)
47. Silling, S.A.: Stability of peridynamic correspondence material models and their particle discretizations. Comput. Methods Appl. Mech. Eng. **322**, 42–57 (2017)
48. Kilic, B., Madenci, E.: An adaptive dynamic relaxation method for quasi-static simulations using the peridynamic theory. Theor. Appl. Fract. Mech. **53**(3), 194–204 (2010)
49. Spagnuolo, M., Barcz, K., Pfaff, A., Dell'Isola, F., Franciosi, P.: Qualitative pivot damage analysis in aluminum printed pantographic sheets: numerics and experiments. Mech. Res. Commun. **83**, 47–52 (2017)
50. Placidi, L.: A variational approach for a nonlinear one-dimensional damage-elasto- plastic second-gradient continuum model. Continuum Mech. Thermodyn. **28**(1–2), 119–137 (2016)
51. Placidi, L., Barchiesi, E.: Energy approach to brittle fracture in strain-gradient modelling. Proc. R. Soc. A Math. Phys. Eng. Sci. **474**(2210), 20170878 (2018)